Chapter 7

Microtopography and Thickness Measurement with Digital Holographic Microscopy Highlighting and Its Tomographic Capacity

Miguel León-Rodríguez, Juan A. Rayas-Alvarez, Amalia Martínez-García and Raúl R. Cordero

Additional information is available at the end of the chapter

http://dx.doi.org/10.5772/66750

Abstract

The refocusing capacity is a unique feature of digital holography. In this chapter, we show the capability of reconstructing digital holograms at different planes for different purposes. One of such purposes is to increase the focus depth of the microscope system. First, we show experimental results of the feasibility to perform digital holographic microscopy (DHM) using a Mirau interferometric objective. A profile phase comparison of a 4.2 μm high microlens using interferometry and DHM, extending the depth of focus of the microscope objective as proof of the proposal, is presented. Second, it is also useful in reducing shot noise when using an LED as a light source. In order to attain the reduction noise, we performed an averaging process of phase and amplitude images reconstructed at different reconstruction distances. This reconstruction range is performed within the focus depth of the optical system. We get a reduction of 50% shot noise. Finally, we show a strategy based on this tomographic capability of reducing a ringing effect by using an ideal filter in off-axis digital holography.

Keywords: digital holographic microscopy, phase-contrast imaging, optical metrology, tomography, phase-shifting

1. Introduction

Digital holographic microscopy (DHM) is a very popular noninvasive testing tool due to its optical nature [1–3]. Many applications use DHM and they have been demonstrated, showing its unique focusing capability; among those applications, micro-electro-mechanical systems (MEMS) and micro-opto-electromechanical systems (MOEMS) analysis demand

higher topographical resolution accuracy [4, 5]. In the inspections of test objects with microscopes presenting some nondesirable phenomena, such as a limited depth of field, aberrations due to defects of optical elements inside the arrangement, optical noise, and parasitic interferences by multiple internal reflections, among others. DHM is not an exception. The microscope has a depth of focus (DOF) limited and as in bright-field microscopy, the areas outside the DOF give out-of-focus and blurred amplitude. Ferraro et al. demonstrated that by DH it is possible to obtain an extended focused image (EFI) of a 3D object without any mechanical scanning, as occurs in conventional optical microscopy [6]. As the unique DHM feature of refocusing works normally, which Ferraro et al. and Colomb et al. demonstrated in their results [6, 7], we can put under inspection MEMS and MOEMS with thicknesses larger than microscope objective (MO) depth of focus. One of the most important challenges in DHM is the reduction of noise. This is because, the lower noise, the smaller will be the measurement error. Different methods have been applied to reduce noise in digital holography. Kang obtained multiple holograms from different angles of illumination by rotating the object or the illumination source. He obtained an improved image through an averaging process [8], similar to the process applied by Baumbach et al. [2]. On the other hand, Rong et al. [9] varied the polarization angle to get an improved image. Also, Charrière et al. [10] applied a method to reduce the shot noise that consisted of averaging multiple holograms in order to get an improved phase image. The noise is reduced by low partial coherence sources. These are usually used, such as laser diodes or light emitting diodes (LEDs) [11, 12]. A disadvantage is their inability to reconstruct the wavefront object for larger reconstruction distances [13]. Here, we present two methods to reduce measurement error in DHM and DH. These methods perform an averaging procedure of phase maps reconstructed at different distances. In addition, we show compensation in the topographical measurement of a 4.2 μm high microlens attained with classical interferometry. This error is due to the limited depth of focus of a Mirau interferometric objective (MIO). In this case, we extend the DOF of the MIO by using the numerical focusing capability of DHM. The last method is based on this tomographic capability of the DHM to reduce a ringing effect by using an ideal filter in off-axis digital holography. We use this capability to get an enhanced image, which is obtained from the spatial averaging method between the focused image at plane ($z = z_{hd0}$) and the first Talbot distance plane ($z = z_{hd1}$). This distance is determined by the period of the ringing phenomenon. Reductions of 50% of these anomalies are computed in simulation and 30% is obtained experimentally (nearly 2 nm). In addition, the simulation results show that the focusing resolution is related with the filter size.

2. Extending DOF of a Mirau interferometric objective by DHM

In this section, we present some experimental results to show how the DOF of a MIO is increased. We show a topographical measurement of a 4.2 μm high microlens attained with classical interferometry. A comparison with the proposal shows the existence of an error. This error is due to the limited depth of focus of the MO. We extend the DOF of the MO by using the tomographic capability of DHM.

http://dx.doi.org/10.5772/66750

2.1. Experimental configuration

The CCD camera records a hologram $I(x, y)$ on the recording plane (x, y). This hologram is the interference between the reference (R) and the object (O) waves. The hologram is magnified by the lens of the microscope (L) (**Figure 1**) and it is given by

$$I(x',y') = \left|O(x',y')\right|^2 + \left|R(x',y')\right|^2 + O(x',y')R^*(x',y') + O^*(x',y')R(x',y'), \quad (1)$$

where the first two terms are the DC term, and the last ones represent the real and the virtual images respectively, while * denotes the complex conjugated.

2.2. Reconstruction of the hologram

Some considerations we need to clarify for the proposal. We must avoid the use of object specimen of low reflectivity because the reference wave cannot be attenuated. The last consideration we have to care about is the dark zone due to obstruction of the reference mirror in the MIO [14].

The most common configurations to obtain $I(x, y)$ in DHM are from either on-line or off-axis. In both cases, we need to tilt the sample (OS) modifying the interference angle between (R) and (O). In the case when this angle is ~0°, the configuration is in-line. This alignment is more accurate than its off-axis counterpart but in the classical way, one needs more images recorded by the CCD camera. We eliminate DC term and the virtual image of Eq. (1), by applying the phase-shifting technique. The filtered hologram $I_F(x, y)$ and the wavefront of the object $U(x, y)$, respectively, calculated from four $\pi/2$ phase-shifted images I_1–I_4 with the four frame algorithm [15]:

$$I_F(x,y) = OR\ \exp\left[i\left(\phi_A + \phi_o\right)(x,y)\right], \quad (2)$$

$$U(x,y) = I_F(x,y)\left(R^*\ \exp\left[-i\,\phi_A(x,y)\right]\right), \quad (3)$$

where ϕ_A is a distribution of system aberrations. Once that remaining aberration of $U(x, y)$ is compensated for, the numerical object wavefront is reconstructed.

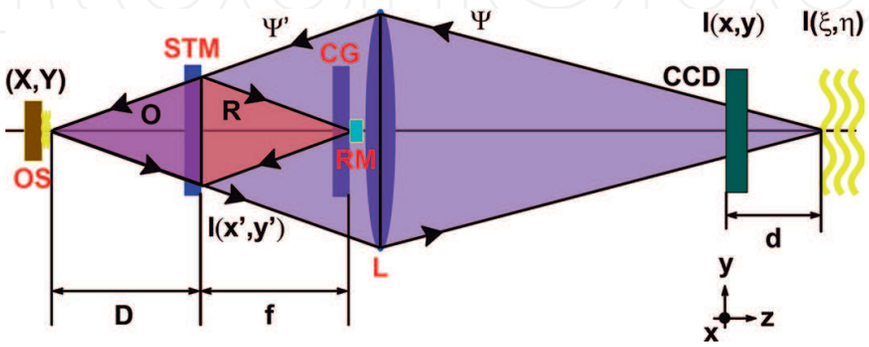

Figure 1. Scheme of the MIO which shows the optical path. L, lens of the microscope; STM, beam splitter mirror; OS, object; CG, compensating glass; RM, reference mirror.

2.2.1. Numerical reconstruction of the wavefront

The wavefront of object $U(x, y)$ is propagated numerically along the optical axis to the image plane (ξ, η), defined by the numerical distance d, according to the angular spectrum method [16].

$$U(\xi, \eta) = \Im^{-1}\left\{\exp\left[ikd\,(1 - \alpha\lambda - \beta\lambda)^{1/2}\right]\left[\Im\ U_0(x, y)\right]_{(\alpha,\beta)}\right\}_{(\xi,\eta)}, \tag{4}$$

where (ξ, η) are the spatial variables, (α,β) are the spatial frequencies, and $\Im$ denotes a two-dimensional continuous Fourier transformation.

The discrete form of Eq. (4) is written as

$$U(m\Delta\xi, n\Delta\eta) = FF\ T^{-1}\left\{\exp\left[ikd(1 - \lambda\, r^2 - \lambda\, s^2)\right] FFT\left[U_0(k, l)\right]_{(r,s)}\right\}_{(m,n)}, \tag{5}$$

where FFT is the fast Fourier transform operator, $\Delta\xi$ and $\Delta\eta$ are the sampling intervals at the observation plane (pixel size), and r, s, m, and n are integers ($-N/2 \le m, n \le N/2$).

The reconstructed wavefront $U(\xi, \eta) = O(\xi, \eta)\exp[i\phi_o(\xi, \eta)]$ provides the amplitude $O(\xi, \eta)$ and phase images $\phi_o(\xi, \eta)$ of the object. From the reconstructed phase distribution $\phi_o(\xi, \eta)$, the specimen topography is determined for the reflection configuration $T(\xi, \eta) = \phi_o(\xi, \eta)/2k$.

2.3. Experimental results

In **Figure 2** is presented the schematic of the digital holographic Mirau microscope (DHMM). The proposed method was carried out using a He-Ne laser of λ = 633 nm in wavelength. The beam is filtered spatially with a spatial filter (SP). The beam goes through a Nikon 50X MIO with a numeric aperture, NA = 0.55. The hologram of sample (S) is imaged on the CCD camera plane by the tube lens (TL). The intensity hologram is recorded by a Pixelink ™ digital camera of CMOS 1280 × 1024 pixels, 8 bits, with a pixel size of 6.7 μm × 6.7 μm. The sample holder is attached with a piezoelectric transducer (PZT) to perform the phase-shifting technique. In addition, this sample holder is attached on an x, y, z displacement and θ rotation stage to perform the sample tilt, which is necessary for the off-axis configuration recording.

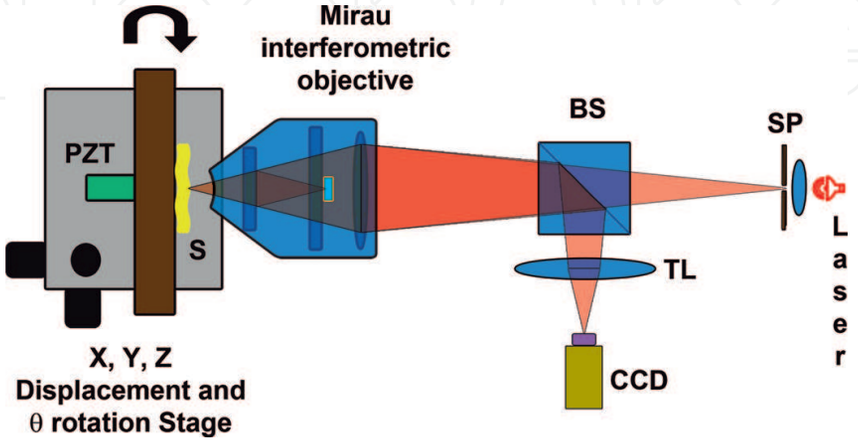

Figure 2. Schematic diagram of the digital holographic Mirau microscope (DHMM).

http://dx.doi.org/10.5772/66750

Now we present one real application of the usefulness of the tomographic capability of DHM. Typically, the MIO is used as a white light scanning and surface profiler in interferometry [14, 17]. In this section, we use this MIO with the DHM and compare the results with interferometry results.

As the tomographic feature of DHM works normally, which was demonstrated in [18], we can put under inspection MEMS and MOEMS with thicknesses larger than MO depth of focus (DOF), as Ferraro et al. and Colomb et al. have demonstrated in their results [6, 7], where this DOF is defined by DOF = $\lambda n_m/NA^2$, where n_m is the refractive index of the medium. We record four shifted holograms of a microlens of 100 μm in central diameter and 4.2 μm in height. **Figure 3(a)** shows a shifted hologram. The reconstruction distance at the top of

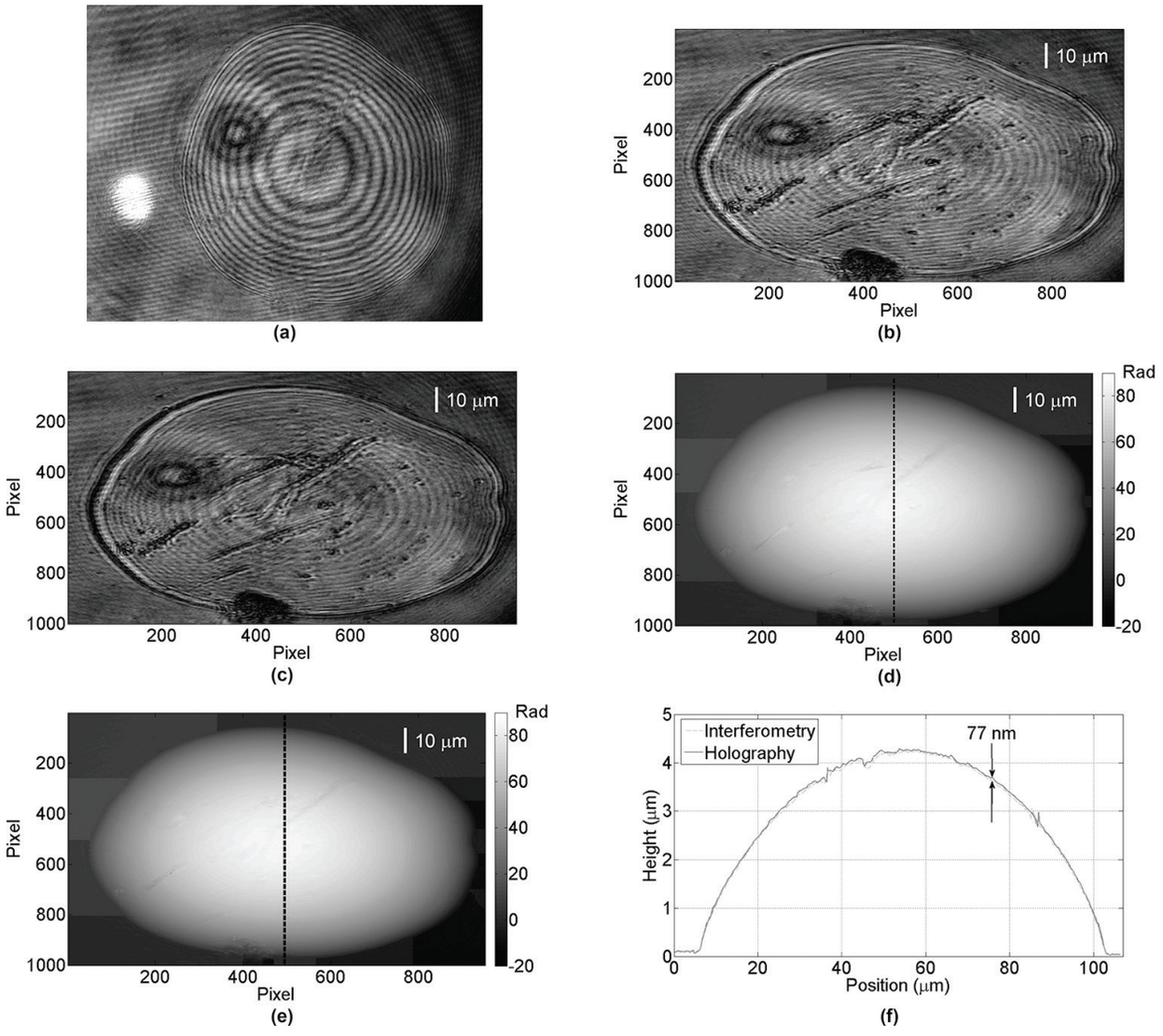

Figure 3. DHM using a MIO applied to a microlens topographic measurement. (a) One of the four-recorded holograms, (b) the reconstructed amplitude image focusing the bottom zone of the object, (c) the reconstructed amplitude image focusing the whole the object, (d) unwrapped phase map applying the phase shifting interferometry method, (e) unwrapped phase map of (c), (f) comparison between profiles measured along the black dash line in both methods, interferometry (d) and DHM (e).

the lens was of 0.4 μm (**Figure 3(b)**). Because the DOF is limited, the areas outside the DOF give out-of-focus and blurred amplitudes. **Figure 3(c)** shows the amplitude distribution map which was reconstructed with the different reconstruction distance method [6, 7] using the MIO and DHM. The initial DOF = 2.09 μm is increased by a factor of 2, as the height of the microlens is about 3.8 μm. **Figure 3(d)** and **(e)** shows both the unwrapped phase images of the specimen by using phase shifting interferometry and DHM methods, respectively. **Figure 3(f)** depicts profiles that compare the phase shifting interferometry result (**Figure 3(d)**) and DHM extending the DOF numerically (**Figure 3(e)**). These profiles correspond to the black-dashed line of the corresponding unwrapped phase map. A difference of about 77 nm is obtained between both measurement methods. The result is in agreement with the results obtained in references [6, 7] for an increased factor of 2. One has to keep in mind that the higher the factor is, the larger the measurement error (difference) will be. Here, we present a measurement system that uses DHM method in order to extend the DOF of the system. Our proposal produces better measurement accuracy due to extended DOF and the numerical reconstruction techniques. With these results, we have demonstrated that it is feasible to perform DHM with the MIO [18].

2.4. Conclusion

We have presented DHMM as a new reliable optical tool for performing DHM in-line reflection configuration. In the experimental results, we have principally proved the unique refocusing capability and the amplitude and phase images of DHM. The object under test sample was a microlens of 100 μm in diameter and 4.2 μm height. With these experimental results, we have also shown that it is possible to extend the DOF of the MO by using the numerical focusing capability of DHM. In addition, we have presented not only DHMM as an alternative to obtain digital holograms without spherical aberration, but also that an easier, well-aligned, and insensitive to external vibrations setup is reached, in comparison with the typical setups. Finally, a topographic measurement error attained with interferometry is demonstrated and compensated with DHM, which is due to the limited depth of focus of the MO.

3. Shot noise reduction in phase imaging of digital holograms

In this section, we show digital holograms with shot noise when they were recorded with a CCD camera. The illumination source used in the optical set up was a commercial LED. Here, we present a technique to reduce the shot noise of the phase and amplitude images coming from a single reconstructed wavefront of the object. To attain a shot noise reduction, an averaging procedure of reconstructed images at different reconstruction distances within the range determined by the focus depth is performed. With this tomographic capacity of DHM, we ensure an improved image without quality diminution, where a noise reduction of 50% is achieved. The results were compared with results from an atomic force microscope (AFM) in order to determine the system accuracy.

http://dx.doi.org/10.5772/66750

3.1. Experimental configuration

3.1.1. LED physical properties

Parasitic interferences and multiple reflections in optical setups are typical; one uses a low coherent source to reduce them. Here, we use a commercial ultrabrilliant LED of 5 mm in diameter, with emission in the red spectrum range. We used a calibrated i1Pro eye-one spectrophotometer of spectral range from 380 to 730 nm. The peak wavelength (λ) measured was of 630 nm, and a full width at half maximum (FWHM, $\Delta\lambda$) of its spectrum was of 24 nm. **Figure 4** shows the typical normalized spectrum of the LED that was used. Then, with the spectral data above mentioned ($\lambda^2/\Delta\lambda$), the coherence length was of 16.5 μm.

3.1.2. Reconstruction process

The experimental setup used was a modified Mach-Zehnder interferometer, as shown in **Figure 5**. When the beam is incident on the diaphragm D of a diameter of 300 μm, spatial coherence is increased. The spatial filter SP with an adjustable diaphragm to limit the source

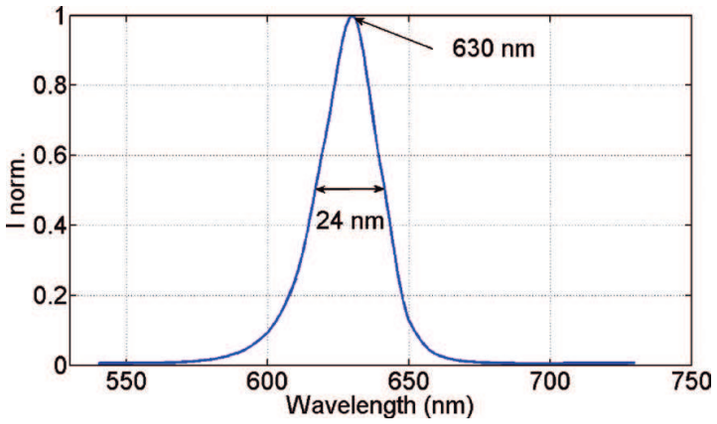

Figure 4. Normalized spectrum distribution of the light intensity emitted by the commercial ultrabrilliant LED.

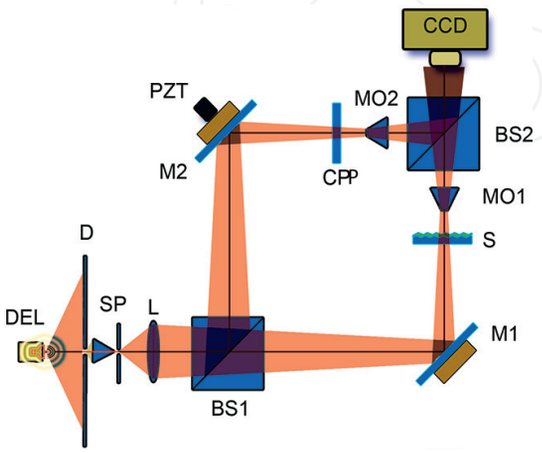

Figure 5. Optical setup implemented on a Mach-Zehnder interferometer with a low coherent source for digital holographic microscopy.

size creates a secondary source of low coherence. The lens L images D at the plane of the sample S and on the compensating plate (CP) when the beam is divided by BS1. The transmitted light through the specimen (S) is collected by a microscope objective (MO1) of 10× with 0.25 of numerical aperture (N.A.), which forms object wave *O*. The object wave interferes with a reference wave *R* when the light is collected by the microscope objective of 10× 0.25 N.A. (MO2) to produce a hologram. The hologram intensity (IH) is recorded by a camera; a CP was inserted in the setup to achieve interference between the two beams (Section 2.3). Also, mirror M1 was mounted on a linear displacement stage with step resolution of 1.25 μm. Mirror M2 was mounted on a piezoelectric transducer (PZT) to implement the phase-shifting technique.

The intensity $I(x,y)$ at the CCD sensor plane is formed by the interference of the object wave $O(x,y)$ and the reference wave $R(x,y)$ as Eq. (1). Mirror M2 is mounted on a PZT to calculate the phase of the initial object using the phase-shifting technique, and to eliminate the DC terms and the virtual image of Eq. (1). The 2π phase module is calculated with the four frame algorithm [15]:

$$\phi_0(x, y) = \tan^{-1}\left[\frac{\left(I_4(x, y; 3\pi/2) - I_2(x, y; \pi/2)\right)}{\left(I_1(x, y; 0) - I_3(x, y; \pi)\right)}\right]. \tag{6}$$

The amplitude of the optical field $A_0(x,y)$ can be obtained by blocking the reference beam and recording only the diffraction object intensity in the CCD plane. Then, the object complex amplitude is as follows:

$$U_a(x, y) = A_0(x, y) \exp\,[\, i(\phi_0(x, y) + \phi(x, y))], \tag{7}$$

where the object wave is determined at the recording (x, y) plane, and ϕ is the phase aberration term.

To reduce phase aberrations induced by misalignment of the optical setup and MOs, we perform the reference conjugated hologram (RCH) method [19]. We obtain the phase aberration term without the presence of the test object, which can be subtracted from Eq. (7) to get the object complex amplitude:

$$U_0(x, y) = A_0(x, y) \times \exp\,[\, i(\phi_0(x, y) + \phi(x, y) - \phi(x, y))]. \tag{8}$$

The angular spectrum method (AS) is performed to calculate the object wavefront at any other plane (ξ, η), in order to refocus it by Eqs. (4) and (5).

3.1.3. Focus depth and averaging method

A limitation in DHM is a limited depth of focus. High magnifications are achievable for investigating microobjects with this technique. However, higher is the required magnification, and lower is the focus depth system. As the geometrical DOF of an imaging system is related to the sampling rate, this DOF is defined as a function of the pixel size and the N.A. of the MO:

$$\text{DOF} = \frac{\Delta\xi}{M^2\,\text{N.A.}}, \tag{9}$$

http://dx.doi.org/10.5772/66750

where M is the magnification.

DHM has as a unique feature that is possible to refocus the object complex amplitude at any plane within the maximum refocus distance [6, 11]. We demonstrate that it is possible to refocus the complex amplitude at different distances within DOF (ΔDOF). The specimen physical thickness is given by

$$h = [\lambda(\Delta\phi/2\pi)/(n-n_0)], \tag{10}$$

where λ is the wavelength, $\Delta\phi$ is the phase step, and $(n - n_0)$ is the index difference between the specimen's material and air.

Shot noise depends on optical power, and it follows a Poisson's statistics [20]. Then we say that a higher light intensity corresponds to a lower shot noise. A way to increase the amount of photons is performing an averaging of the reconstructed images in order to attain an improved image.

We performed an averaging process of the reconstructed images that are obtained from different reconstruction distances within the system's DOF in order to get an improved image. These reconstructed images are uncorrelated with each other at specific reconstruction distances, and computed from the same complex amplitude [21].

We think that if these reconstructed images are uncorrelated with similar standard deviations $STD_{c'}$ one can write the following for the standard deviation of an averaged image $\sigma_{\bar{x}}$:

$$\sigma_{\bar{x}} = \frac{1}{\sqrt{C}} STD_{c'} \tag{11}$$

where C is the number of images to average.

If four images are averaged, theoretically, noise reduction is of 50%.

3.2. Numerical and experimental results

In this part, the results of the recorded holograms are presented. The shutter camera enables us to reduce the exposure time down to 40 μs, with a variable gain from 0 to 17 dB in 14 increments. We do not reach a camera's full well capacity with a LED source in the setup presented, even with the maximum integration time and no electrical gain of camera parameters [21]. The optical power of the intensity was measured with a photo detector. First, a comparison between a blank experimental hologram and the simulated hologram results is shown. The intensity of the blank holograms was of 6.7×10^{-15} W/cm^2, and this corresponds to an average number of 5100 of photons per pixel. **Figure 6(a)** presents a blank phase image that is reconstructed without a phase aberration correction. A standard deviation (STD) = 12° is computed in the black square area. On the other hand, **Figure 6(b)** presents the same reconstruction after the RCH method was applied, with a STD = 0.7° in the same area.

We have noncorrelation among phase images reconstructed at different distances [21]. These images were obtained of the recorded experimental holograms from Eq. (4). **Figure 7** shows that when there is a difference of distance of 2 μm from one reconstructed phase image to

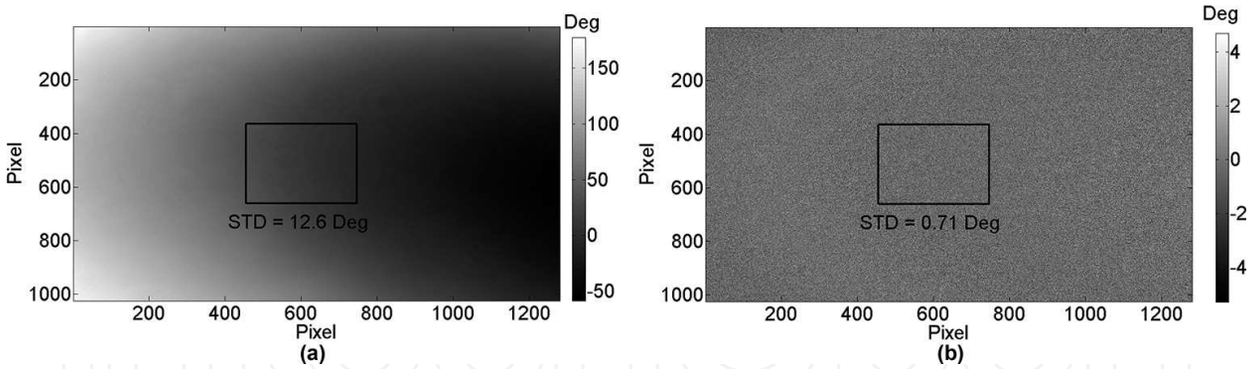

Figure 6. Reconstructed phase image from a recorded hologram without any sample. (a) Phase image without aberration correction and (b) phase image with aberration correction.

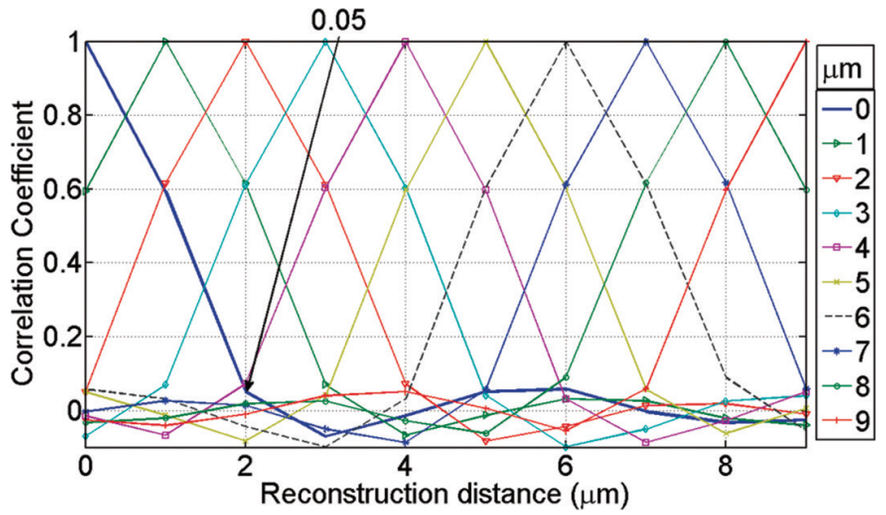

Figure 7. Correlation coefficient between reconstructed phase images at different reconstruction distances from the same wavefront of holograms recorded with low intensity (photons per pixel of 5100).

another one obtained from same complex wavefront, a noncorrelation exists between these images. In that case an averaging procedure can be performed of these noncorrelated images in order to get an improved image. These results validate the proposal previously demonstrated in reference [21].

With the Δd = 2 μm calculated, we can average C images. In **Figure 8(a)**, the phase image is shown without any averaging. This image was reconstructed within DOF of the system with d = 30 μm. The STD in this phase image is of 0.69°. On the other hand, **Figure 8(b)** shows a phase image after applying the proposed averaging procedure with 10 phase images. The STD of this image is of 0.231°. We get an image improvement of 68.4% of noise reduction. This is in agreement with Eq. (11). A profile comparison is shown in **Figure 9(a)**. The profiles were taken for the marked profile as a white line in the phase images in **Figure 8**.

Figure 9(b) presents the behavior of the STD as a function of the number of phase images C used in the averaging procedure. Also, a comparison between numerical simulation results and

http://dx.doi.org/10.5772/66750

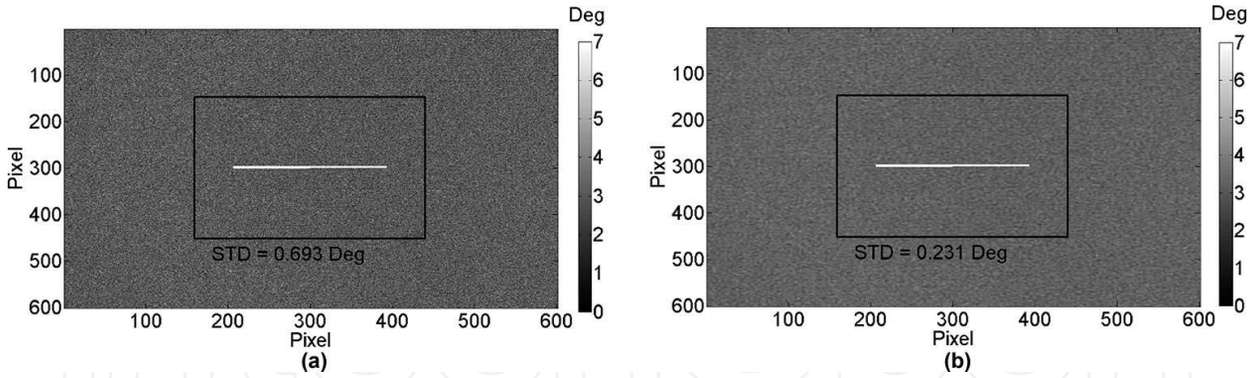

Figure 8. Improvement of phase image by the proposed averaging method in DHM. (a) Reconstructed phase image within DOF of the system and (b) phase image improved from 10 averaged phase images reconstructed.

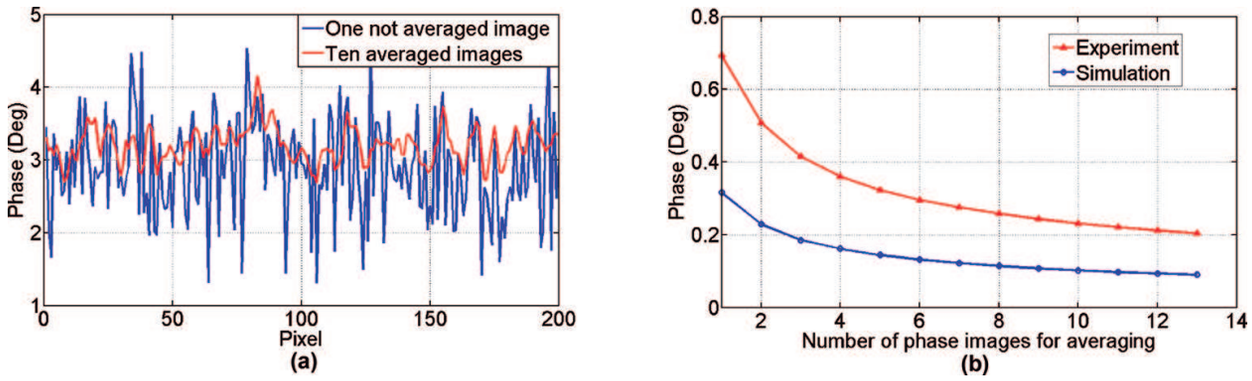

Figure 9. Behavior of noise phase reduction when, the averaging method is applied. (a) Profile of phase images in **Figure 8**, where a diminution of STD when 10 phase images are averaged and (b) profile of phase STD as a function of the number of phase images, where a behavior of $C^{-1/2}$ is shown in the STD reduction [21].

experimental results is presented. The simulation results were attained with a 5100 photons per pixel. The behavior of the shot noise reduction in experimental results follows the expected theoretical function defined in Eq. (11). Then we can say that the averaged images are noncorrelated. The difference, presented between experimental and simulations results, is due to the presence of sources of noise other than shot noise, quantum efficiency, and small optical defects in the optical components. One can see that if the number of averaged images increases, the offset also decreases. Noise sources should be speckle and thermal noise of CCD camera. Both the integration time during hologram recording is not the highest and the camera's well capacity is not reached due to low illumination, therefore the noise related to the quantum efficiency of the CCD detector is the main factor which is the difference between the experimental and simulated results.

3.2.1. Decrease of shot noise in amplitude images

A principal limitation in the proposal is limited DOF. As we have already seen in Section 3.1.3, DOF is related with the sampling distance and numerical aperture of the optical system. In the system described, the theoretical DOF is of about 0.268 μm. But, in the experimental

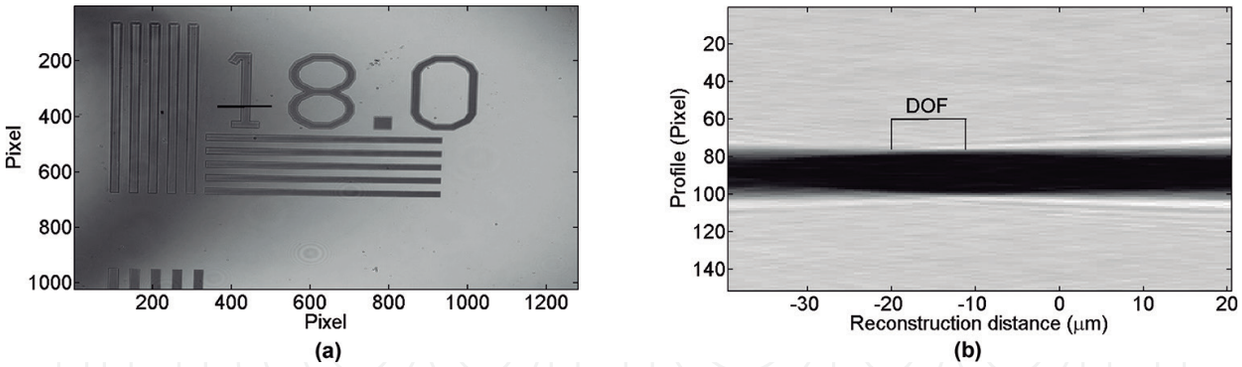

Figure 10. Determination of the DOF experimentally. (a) Recorded hologram and the profile zone taken to measure the DOF and (b) evolution of intensity when reconstruction distance is increased.

reconstruction, DOF is higher than would have been expected from Eq. (9). This is because the fact that the spatial resolution (pixel size) introduced by the optical setup is limited [13]. To experimentally attain the DOF, in **Figure 10(b)**, we have plotted a line profile shown in **Figure 10(a)**, where the profile is marked with a black line. The evolution of this plot starts at 40 μm before the image is focused. After zooming on the focus zone, we can determine that the DOF is 9 μm. The test object we used was an Edmund NBS 1963A resolution card. The zone of interest corresponds to 18 double lines per mm (lpmm). The reconstruction distance was of 15 μm.

If the DOF is 9 μm and Δd is of 2 μm, then we can average four images to carry out what we propose. These images have to be reconstructed at a distance within DOF to guarantee that image quality is not affected. **Figure 11** shows the image improved when the proposed method is applied. This evaluation is through STD in the area defined by the white square in each image. We attain a STD = 1.57 gray levels (GL) for an image focused without averaging (**Figure 11(a)**), and STD = 0.869 GL by applying the proposal method (**Figure 13(b)**). Then we say that the averaging process that we propose also improves the amplitude image.

In order to show that the lateral resolution is not affected by the averaging method that here is proposed, we have plotted a line profile marked by the white lines in **Figure 11**. **Figure 12**

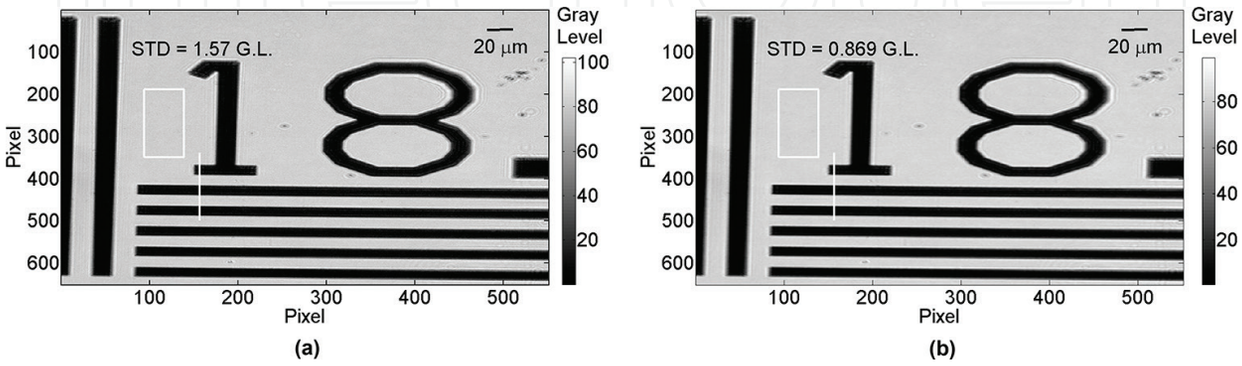

Figure 11. Reconstructed focused amplitude images. (a) Reconstructed focused amplitude image without averaging and (b) reconstructed amplitude image when the averaging process is performed with four focused amplitude images.

http://dx.doi.org/10.5772/66750

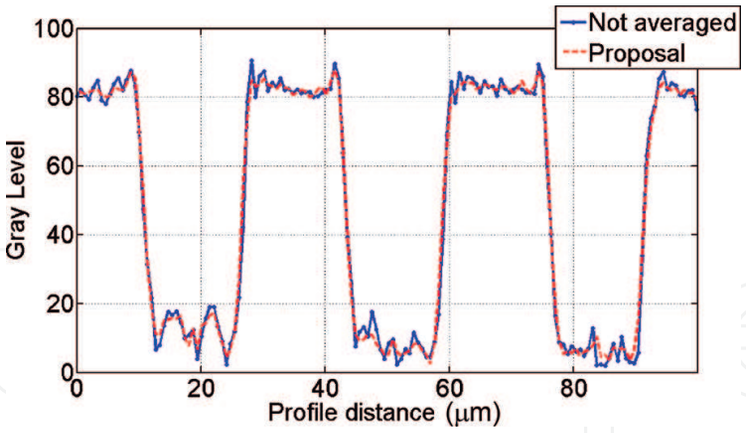

Figure 12. Comparison between profiles measured along the white lines defined in **Figure 11(a)** and **(b)**.

shows this plot and the comparison between the focused amplitude image without averaging and the improved image after applying the proposed method.

We can note, from this comparison in **Figure 12**, that there is no difference in the transition edges. On the other hand, we can clearly note the improvement on top and bottom areas from these profiles where the STD of the proposal clearly is the lowest.

3.2.2. Decrease of shot noise in phase images

First, we use a 100 nm step-wise specimen made at home of TiO_2 thin film, with a refraction index of 1.82 for a wavelength of 632.8 nm, as a phase-calibrating gauge. The specimen was made using a Balzer B-510 vapor deposition machine. To ensure a real and accurate measurement reference, the test object was measured with a Digital Instruments 3100 AFM. **Figure 13(a)** shows the reconstructed phase image of the step-wise, where the reconstruction distance was of 10 μm. The STD measured in the zone enclosed by the black square is of 3.44 nm. After applying the averaging proposal of four reconstructed phase images at $\Delta d = 2$ μm inside DOF, we compute a reduction of about 1.24 nm (corresponding to 0.57° of STD reduction). **Figure 13(b)** shows the improved phase image in comparison with the predicted value of the experimental results, where the STD reduction was of 0.35 deg (**Figure 9(b)**). This is because the higher than expected SDT reduction is mainly due to a lower intensity recording than the blank recorded holograms. This lower intensity is due to the glass plates thickness located in the arms of the interferometer (4.7 mm glass of each). There are some other causes that generate noise in the phase image, such as quantum efficiency of CCD and small optical defects in the optical components, Thermal noise of CCD, among others. The noise generated by these causes is also reduced in a percentage. The evaluation zone is marked in **Figure 13(b)** by the white solid square. In **Figure 13(d)**, we present the topography measurement, which was done by AFM. Normally, this measurement needs to correct it by a numerical procedure. This is due to a tilt contribution in one or both lateral directions. In **Figure 13(c)**, we present the zone where the comparing information was taken of the improved phase image by zooming in the white dashed rectangle of **Figure 13(b)**. A profile comparison extracted from the white lines in **Figure 13(c)** and **(d)** is presented in **Figure 14**. These profiles show their topographic

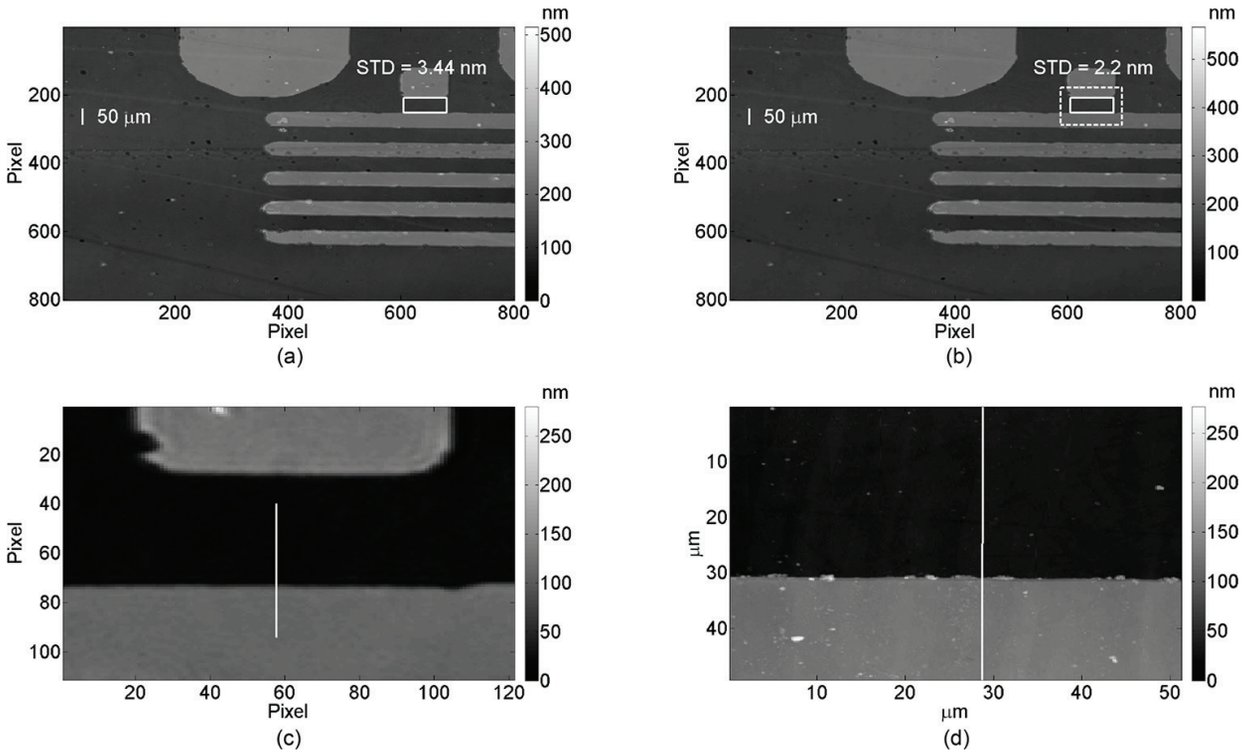

Figure 13. Topographic measurement of the TiO_2 step-wise specimen. (a) One reconstructed phase image, (b) improved phase image when the averaging process is performed, (c) corresponding zoomed area inside the white dashed rectangle in (b), and (d) numerical data extracted from AFM.

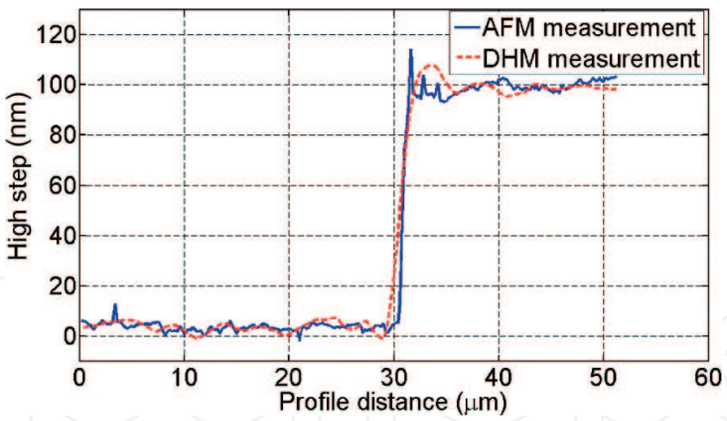

Figure 14. Comparison between profiles measured along the white lines defined in **Figure 13(c)** and **(d)**.

heights. The biggest difference is mainly located in the transition zones. This difference is due to differences in the lateral resolution between microscopes. It can also be improved in the upper and lower areas with topographic measured while the AFM (blue solid line), due to what has been discussed above. DHM must be reached in larger lateral resolution by using an MO with high NA., this makes our proposal is a comparable alternative method with AFM [21]. Furthermore, the method has some advantages DHM against AFM. One of them is the time to obtain topographic data, because while our proposal takes just seconds to perform the

http://dx.doi.org/10.5772/66750

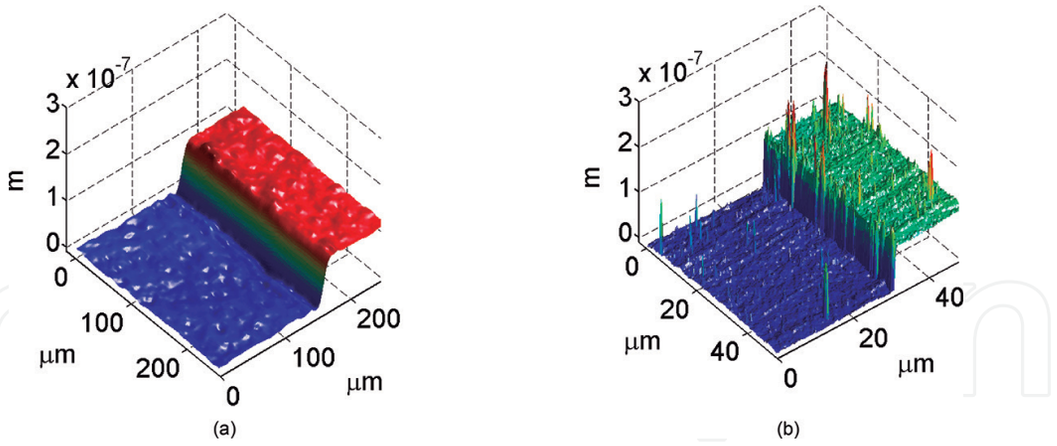

Figure 15. 3D TiO_2 step images. (a) Topographic measurement done by AFM and (b) topographic measurement enhanced through the averaging process done by DHM.

topography, AFM measurement takes several minutes to complete this task. Another advantage is the flexibility to test an area larger than the AFM method. A last important advantage of our proposal is that it is cheaper in their application that the AFM.

Finally, **Figure 15(a)** and **(b)** present the 3D topographic map of the TiO_2 step presented in **Figure 13(d)** and **(c)**, respectively. **Figure 15(a)** corresponds to the data provided by the AFM. The smaller sampling rate commented above has a better ability to detect defects in the sample. **Figure 15(b)** corresponds to an improved topographic data obtained by DHM.

3.3. Conclusion

In DHM the phase information has great importance for the analysis and characterization of materials, such as biological samples and microoptical systems. In this study we have shown a different way to get an improved topographic measurement. The proposal is based on the decrease of the shot noise in DHM. In this section, we show a proposal that is based on the averaging process of reconstructed images by the tomographic capacity of DHM within the range determined by the focus depth. We obtained an improved phase image without quality diminution, in which a noise reduction of 50% was achieved. In addition, we have been shown axial topographic measurements in agreement with the measurements made with a standard AFM.

4. A method to reduce the ringing effect in phase imaging in off-axis digital holograms

In this section, we present a method to reduce the ringing effect of discontinuous surfaces in the reconstruction process in off-axis digital holography. The method is based on the natural diffraction of light (Talbot effect). We previously showed that for variable grating, Talbot phenomenon is also present [22]. When you use a binary filter in order to attain the object-wave in off-axis digital holography, this allows an easy implementation of filtering mask in the filtering process. By using the binary filter the appearance of Gibbs phenomenon in discontinuous

surfaces appear. However, such a phenomenon was possible to reduce (experimentally nearly to 2 nm) by using the unique feature that digital holography have, this is the tomographic capacity. In addition we show that the size of the binary low-pass filter in the holographic reconstruction process is related to the focus zone. The versatility by using binary low-pass filter allows us to fit size according to the sample under study. It is possible with the tomographic capability chose the interest zone in axial direction to inspect the sample. This allows us while applying the low-pass filtering process to avoid the defects that can occur on either the optical component or the sample container. The results should be of interest to readers in the areas of optical metrology, grating diffraction, digital holography, and digital holographic microscopy.

4.1. Proposal of the method

The optical setup used in the present study for recording off-axis digital holograms is a Michelson interferometer presented in **Figure 16**. The light source is from a laser diode with a wavelength of 643 nm, which is expanded by a beam expander system (BE). This source is linearly polarized plane wavefront with short coherence (coherence length about 0.1 mm). The beam is split by a beam splitter (BS) into a reference wave *R* and an object wave *O*. The CCD camera records an off-axis hologram at the exit of the interferometer. This hologram (*H*) is created by the interference between the $O(x,y)$ and $R(x,y)$, after they reflect on the sample (S) and mirror (M), respectively. To obtain off-axis holograms, the orientation of M is set in such a way that, the CCD is reached by $R(x,y)$, with an incident angle θ, while $O(x,y)$ is perpendicularly propagated with respect to the hologram plane. The distance *z* between the CCD and the object is 85 mm. The CCD is a standard black and white camera with pixel size of 4.4 μm and 8 bits of depth.

This off-axis digital hologram $H(x,y)$ can be expressed by the Eq. (1). A window function $W(f_x,f_y)$ is used to filter the term $O(x,y)R^*(x,y)$ of Eq. (1) in the frequency domain. On the other hand, the so-called frequency spectrum filtering method [23] is applied in order to retrieve the object wavefront $O(f_x,f_y)$. Here,

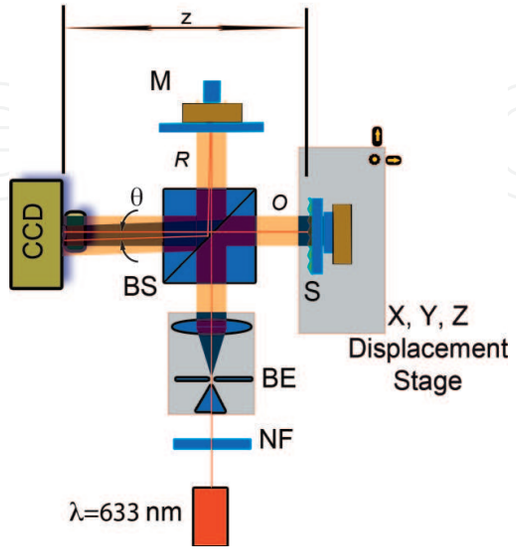

Figure 16. Optical system based on a Michelson interferometer. M is a mirror, NF is a neutral filter and BE is a beam expander.

http://dx.doi.org/10.5772/66750

$$O(f_x, f_y) = W(f_x, f_y)\ \Im^{\mp 1}\{H(x, y)\ R_D(x, y)\}, \tag{12}$$

where R_D is a digital replica of R, and $\Im^{\mp 1}$ stands for either the direct continuous Fourier transform or its inverse counterpart, in other contexts. Hence, the object $O(f_x, f_y)$ can be propagated using the approximation of the Fresnel-Kirchhoff propagation integral as follows [16]:

$$O_i(x, y, z_i) = \Im^{+1}\left\{\begin{array}{l}\left[O(f_x, f_y)\right]\exp(jk\, z_i) \\ \times \exp\left[-j\pi\lambda\, z_i\right]\left[(f_x)^2 + (f_y)^2\right]\end{array}\right\}, \tag{13}$$

where λ is the wavelength, k is the wave number and z_i is the reconstruction distance. The reconstructed object wavefront $O(x,y)$ provides the amplitude image $A_i(x, y)=|O_i(x,y)|^2$ and the phase image $\phi_i(x,y)=tg^{-1}(imag(O_i(x,y))/real(O_i(x,y)))$ of the object. The topography $T(x,y)$ of the specimen is computed from the reconstructed phase $\phi(x,y)$, by the reflection configuration $T(x,y) = \phi(x,y)/2k$.

4.1.1. The Fourier filtering process

The filtering process is a well-known technique outlined by Cuche et al. [23]. However in this proposal the *DC* term is eliminated by the subtraction of the intensity of *R* and *O*, recorded independently, in Eq. (1). Edges and other sharp transitions (such as noise) in the digital hologram contribute significantly to the high-frequency content of its Fourier transform [16]. We considered three types of low-pass filters: ideal (ILPF), Butterworth (BtwLPF), and Gaussian (GLPF). These three filters cover the range from very sharp (ideal) to very smooth (Gaussian) filter functions. When we use the ILPF, a ringing effect appears at the sharp transitions zone of the reconstructed image due to transfer function *W* in Eq. (12); which is a *sinc* function. In addition, the filter size (cut-off frequency) is directly related to the period of the ringing [24, 25]. On the other hand, since the transfer function of the Gaussian filter is also a Gaussian function, it will have a blurring behavior, but no ringing effect. When you use the BtwLPF of second order, the ringing effect and the blurring is similar to that observed in the Gaussian filtering. Then the ringing increased, according to the order of the filter as we commented in [22].

4.1.2. The Talbot effect

When a monochromatic wavefront is plane and illuminates a linear grating of period *p*, multiple identical images of the original grating are observed along the propagation axis of the light. These images are formed without any lenses on multiples of the Rayleigh distance (z_{tdu}). This phenomenon is known as the Talbot effect or self-imaging and it is due to the diffraction of light when pass through the grating [26]. The Talbot distance is located at:

$$z_{tdu} = \frac{up^2}{\lambda}, \tag{14}$$

where u = 1, 2, 3,… denotes the Talbot plane order (TPO) and λ is the illumination light wavelength. When u is odd the self-imaging has 180° phase shift and contrast reversal [16]. The same result can be present in a thin phase attenuated sinusoidal grating as we presented in [22].

4.2. Simulations

A simulation was performed to get an off-axis digital hologram. According to the optical scheme (**Figure 16**), two plane waves of equal intensities have been considered to interfere in a Michelson interferometer for attaining off-axis digital hologram. We design a synthetic object, which consists of three horizontal bars and three vertical bars etched on a thin chromium film (100% reflective) deposited in a glass substrate. The reflectance of the film is of 6.25% and the thickness of 0.7π rad. (**Figure 17(a)** and **(b)**). In real world the reflectivity of 100% of an object is not possibly reached, but the simulation allows us to design synthetic objects with 100% reflectivity. The size of this object is of 1200 × 1200 pixels; the distance between the object and the CCD plane is of z = 84.4 mm. We assumed a red wavelength of 643 nm from a laser, and pixel size of 4.4 μm × 4.4 μm of the CCD according to the real parameters. If we consider a wavelength of 643 nm then the sample thickness will be of 112.5 nm by applying the topographic formula that was mentioned at the end of Section 4.1. We have considered the standard deviation (STD) as a measure of the axial resolution and amplitude improvement (arbitrary unit [a.u.]) in all sections. **Figure 17(c)** present the synthetic off-axis digital hologram.

We start reconstructing the object wavefront by performing the Eq. (13) with a reconstruction distance ($z = z_{td0}$) of 84.4 mm. To remove the DC term and the virtual image, we perform the Fourier filtering process mentioned in Section 4.1.1. **Figure 18(a)** and **(b)** presents the amplitude and phase images, respectively, by using an ILPF with a cut-off frequency of radius of 100 pixels. As we have been mentioned, **Figure 18(a)** shows a profile where the ringing effect appear with a period of u = 53 μm. This profile is comparable to a variable transmittance function (VTF) grating simulated, according to Goodman [16] and confirmed in previous simulations [22] with the 180° phase shift and contrast reversal of the field distribution at the first TPO (z_{td1}) property. Next a second reconstruction was performed at $z = z + z_{td1}$ = 88.7 mm with the same size of the filter. It should be noted that normally the reconstruction of the object wavefront is done only at one distance; this is the focusing distance z. However, to reduce the ringing effect we need to perform an averaging operation between phase and amplitude reconstructed images at different distances z_{ht0} and z_{ht1} that is:

$$\begin{aligned} \phi(x,y) &= [\phi_0(x,y) + \phi_1(x,y)]/2 \\ A(x,y) &= [A_0(x,y) + A_1(x,y)]/2. \end{aligned} \tag{15}$$

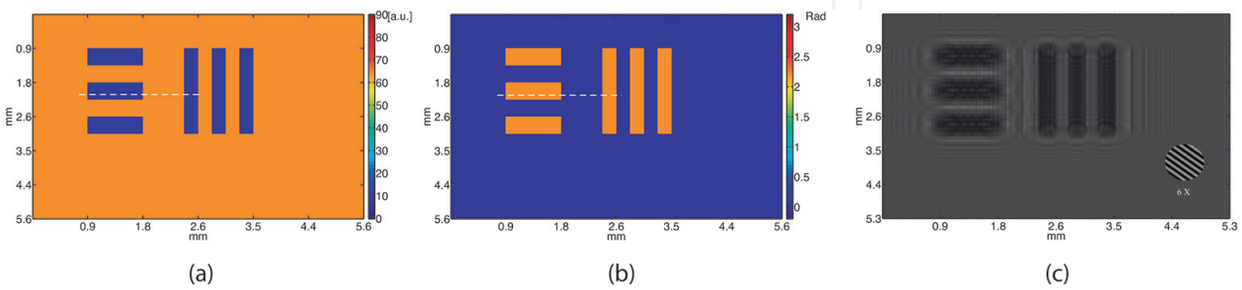

(a) (b) (c)

Figure 17. (a) Amplitude and (b) phase test object used to perform numerical simulation, and (c) off-axis digital hologram recorded at z = 84.4 mm from the object test.

http://dx.doi.org/10.5772/66750

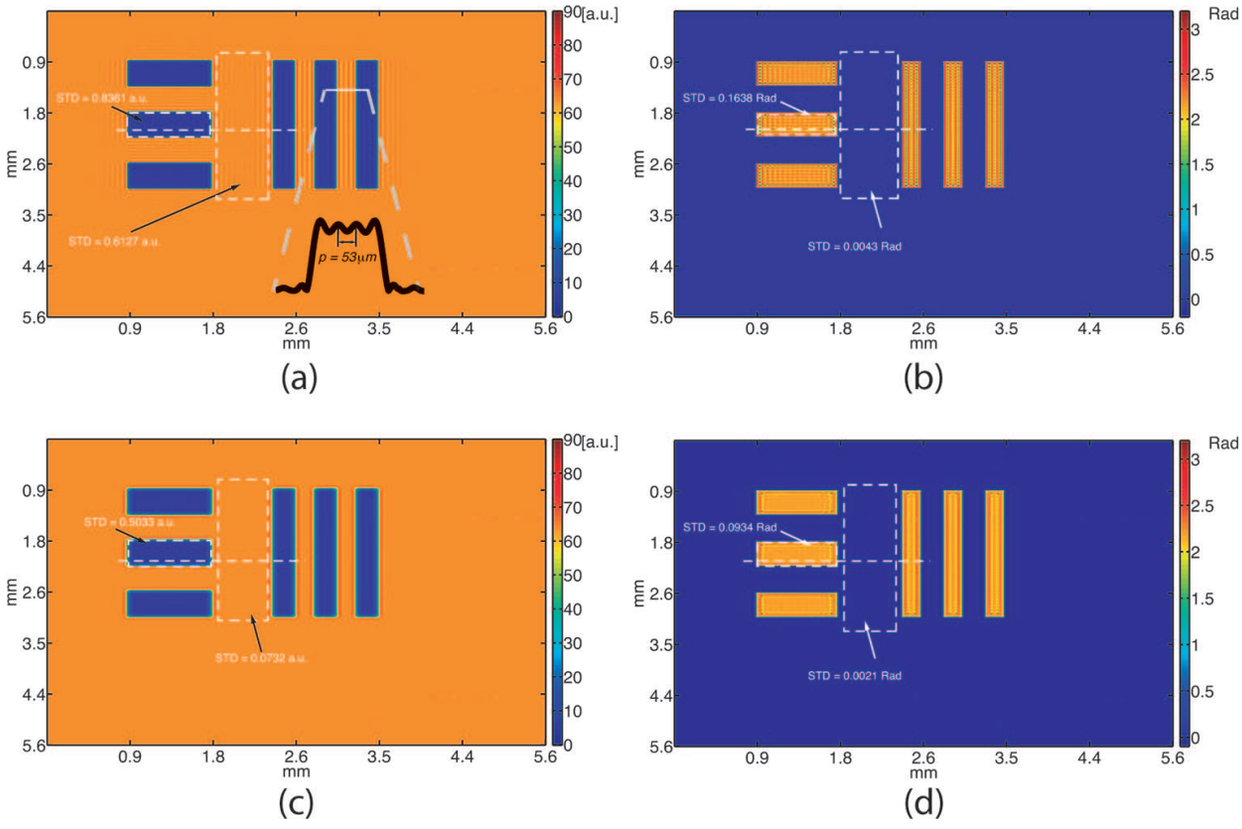

Figure 18. Reconstructed images from the hologram of **Figure 3(c)**. (a) and **(b)** Reconstructed amplitude and phase images at $z = z_{td0}$ respectively, (c) and (d) improved amplitude and phase images, respectively, after proposal is applied.

From **Figure 18(c)** and **(d)**, we can see the both improved images amplitude and phase map, obtained with this proposal. A comparison between the corresponding images obtained at a single distance of reconstruction z and our proposed method is done. We can note a clearly noiseless images reconstructed by our proposal. The improvement with this procedure is an average decrease of STD of 64% in the amplitude image and 47% in phase image. The percentage is an average between the two zones delimited by the dashed rectangles in **Figure 18**. The STD of the region of interest is represented in each reconstructed images. As far as we know this is a new and useful method to reduce the ringing phenomenon.

In **Figure 19(a)** and **(b)**, we show line profiles taken from white-dashed line shown in **Figures 17(a)–(b)** and **18(a)–(d)**. Also, we have included profiles from reconstructed images at the first TPO and profiles from reconstructed images when Gaussian and Butterworth filters were used in the filtering process. We can appreciate the periodic property as a result of using an ideal filter not only at z_{ht0} but also at z_{ht1}. We can note this behavior in both amplitude and phase distributions. Additionally, and in agreement with simulations performed in [22], we can observe not only a phase shift of 180° and reversal amplitude attained in the reconstruction at z_{ht1}. An unfavorable anomaly, but usual, phase, and amplitude variances are presented in boundaries (edges) due to single diffraction order that does not superpose with other diffraction orders [27]. Due to that, when the averaging is performed between reconstructed images at z_{ht0} and z_{ht1}, we cannot compensate the ringing in this zone. On

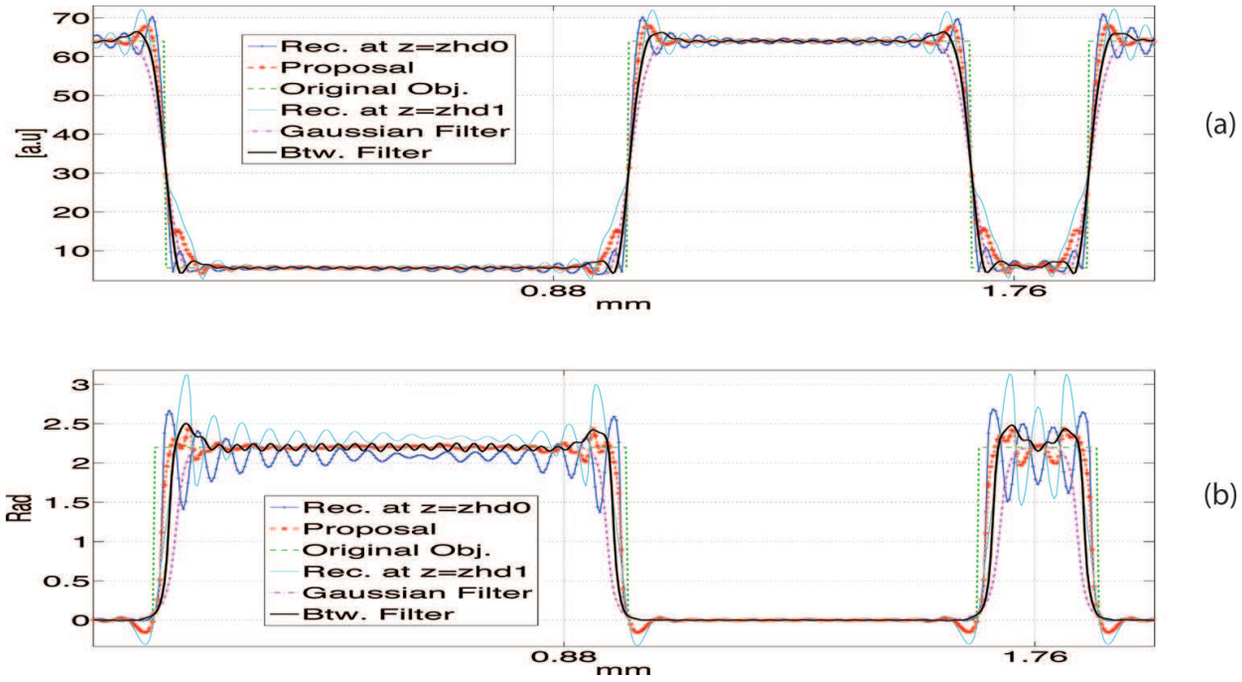

Figure 19. Comparison between profiles measured a long white dashed line of **Figures 3(a)**, **(b)** and **4(a)–(d)**. **(a)** Profiles of amplitude distributions and (b) profiles of phase distributions.

the other hand, we observe a loss of lateral resolution in reconstructed images (principally in phase distribution) when BtwLPF and GLPF are applied in the filtering process. This is important to know as phase distribution is directly related with thickness and, in our case, sample topography.

Nevertheless we can see a slight difference between proposal and the BtwLPF of second order in the profiles comparison. However, an advantage of ideal low-pass filter is that have the possibility to increase the tomographic resolution. This property is due to pixel size, magnification, and numerical aperture of the optical imaging system as demonstrated by Dubois et al. [13] and in our case, the filter size. To illustrate the determination of tomographic zone (TZ), in **Figure 20(a)** we have plotted the intensity evolution with the reconstruction distance on a line profile from the **Figure 18(a)**, where the profile zone is marked with a white-dashed line. The starting image is defocused by -10 to 10 mm. We can see that the TZ is of 3.2 mm by using the ideal filter and 16 mm by using the Butterworth one. Then we say that ideal filter is better to determine a focus zone than Butterworth. This result permit us not only to determine the best and most accuracy reconstruction distance zone to prevent measurement errors [28], but also to adjust the tomographic capability with respect to the sample thickness to reduce the defects that can occur on either the optical component or the sample container. Also this capacity helps us to control the resolution of plane scanning in a tomographic scheme [13]. **Figure 20(c)** presents the intensity evolution of the line profile in the zone marked with white-dashed line as **Figure 20(a)** but with filter size of 200 pixels of radius. This shows a smaller focus zone than a filter size of 100 pixels of radius (**Figure 20(a)**) evidencing the above mentioned.

http://dx.doi.org/10.5772/66750

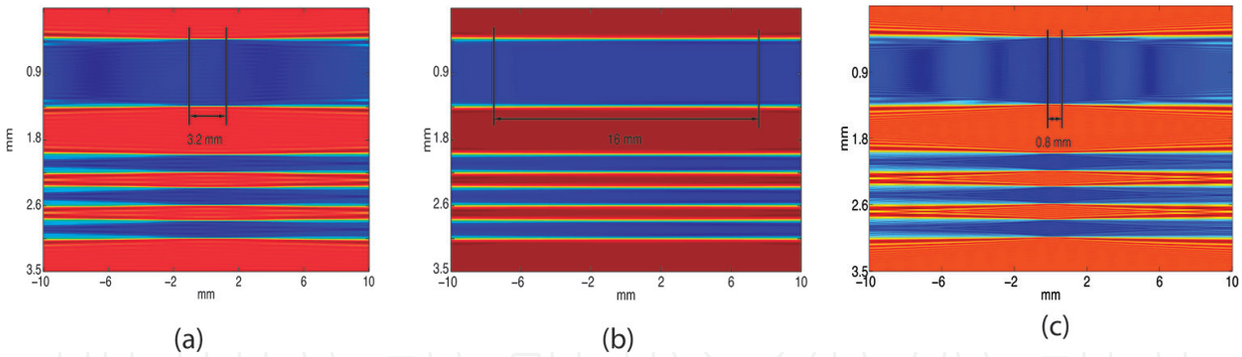

Figure 20. Evolution of intensities determined on a profile line when reconstruction distance is increased. Using (a) an ILPF of 100 pixels of radius, (b) a BtwLPF of 100 pixels of radius and (c) an ILPF of 200 pixels of radius.

4.3. Experimental results

In this section, we present experimental results of the recorded holograms of 1600 × 1200 pixels size. **Figure 15** shows the digital holographic setup that we implement. We use a laser diode of 643 nm in wavelength as light source. This source is a diode of low coherence (about 0.1 mm) linearly polarized plane wavefront to prevent parasitic interference and optical noise. The hologram is recorded by a CCD Pixelink™ digital camera of 1600 × 1200 pixels, 8 bits, with a pixel size of 4.4 μm × 4.4 μm. The sample holder is supporting on an x, y, z, displacement and θ rotation stage to perform the sample tilt, which is necessary for the off-axis configuration recording. We used an USAF 1951 resolution test target in the zone that corresponds to the 1-1 test group as the object test. In **Figure 21**, we show a recorded digital hologram [22].

At the beginning, we reconstructed the object wavefront by performing the Eq. (13) with a reconstruction distance ($z = z_{td0}$) of 85 mm. **Figure 22(a)** and **(b)** shows the amplitude and topography distributions, respectively, by using an ILPF with radius of 100 pixels (cut-off frequency). As ILPF size is the same, as used in simulations results, then a ringing artifact with a period of u = 53 μm appear in the reconstructed images. A second reconstruction was

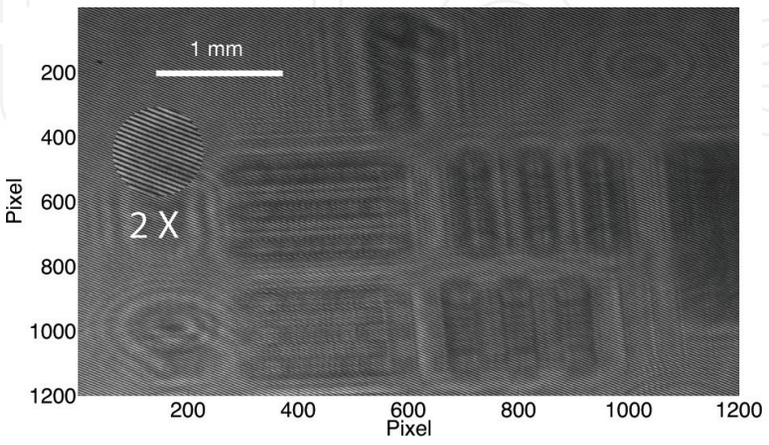

Figure 21. Digital experimental hologram of the USAF 1951 resolution test target.

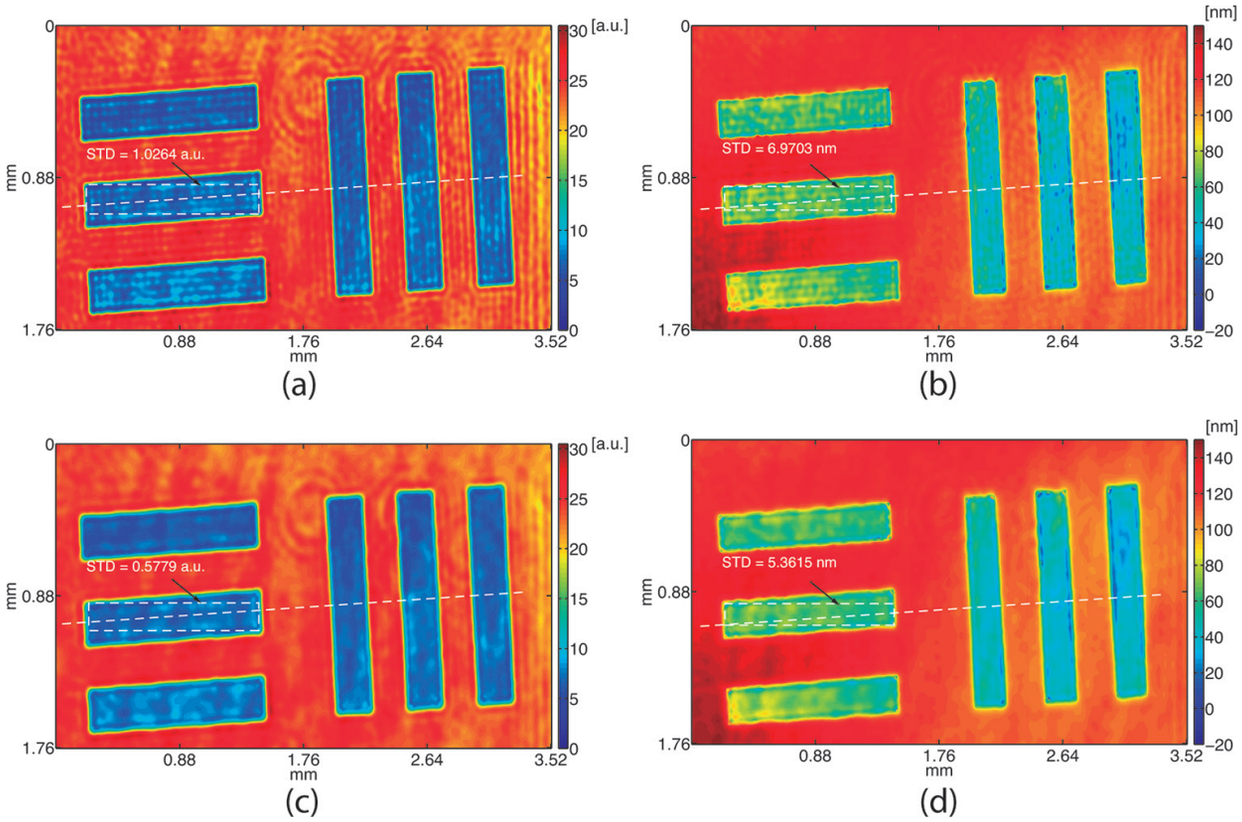

Figure 22. Reconstructed images from the hologram of **Figure 7**. (a) and (b) Reconstructed amplitude and topography distributions at $z = z_{td0}$ respectively, (c) and (d) improved amplitude and topography respectively after proposal is applied.

performed at $z = z + z_{td1}$ = 89.4 mm. To reduce the ringing effect we perform the averaging proposal between phase and amplitude reconstructed images, as we previously mentioned. In **Figure 22(c)** and **(d)**, we present the enhanced images obtained with this proposal. The improved distributions contain nearly all the details of the original object. The reduction with this procedure is an average of 43.7% of STD in amplitude image and 23.1% in the topography. The percentage is an average between the two zones delimited by the dashed-white rectangles in **Figure 22**. **Figure 23(a)** and **(b)** presents line profiles where region is marked with a white-dashed line shown in **Figure 22(a)–(d)**. Also, as simulation results, we have included profiles from reconstructed images at the first TPO and profile from reconstructed images when Butterworth filter is used in the filtering process. We can note the periodic component as a result of using an ideal filter at z_{ht0}. This behavior is presented in both amplitude and phase distributions in agreement with simulation results. We assume that the percentage difference between simulation results and experimental results is principally due to an additional low frequency noises coming from optical devices defects, a nonperfect plane wave reference, aberrations noncompensated, and also a nonuniform thin film deposited on target. Nevertheless, we can see a difference between proposal and the BtwLPF of second order in the profiles plot exactly as in simulation performed in [22]. These differences are mainly at the transition edges, which are related to the lateral resolution.

http://dx.doi.org/10.5772/66750

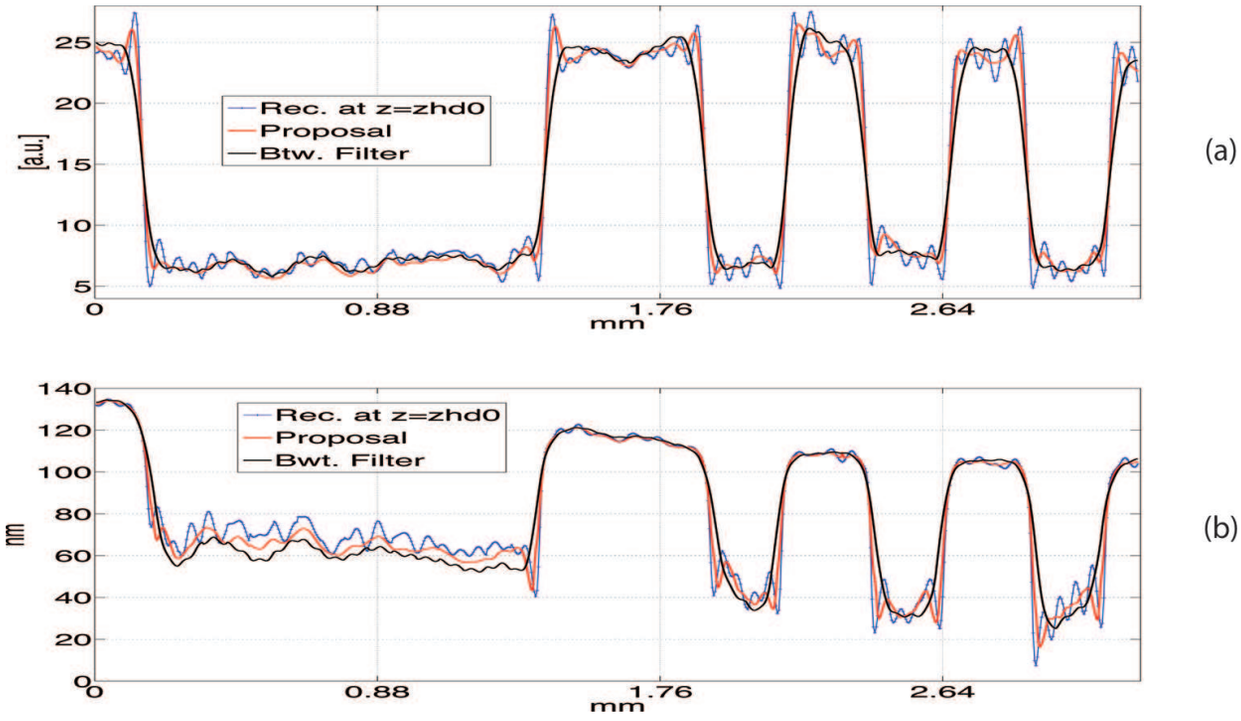

Figure 23. Comparison between profiles measured a long white dashed line of **Figure 8(a)–(d)**. (a) Profiles of amplitude distributions and (b) profiles of topography distributions.

4.4. Conclusions

In this work, we present a new method to reduce the ringing effect of discontinuous surfaces reconstruction in off-axis digital holography. The technique is based on the diffractive nature of light (Talbot effect). We use an ideal filter in the filtering process in digital off-axis holography, because it allows an easy implementation and versatility to choose frequencies of interest. The major disadvantage in using this filter is the appearance of Gibbs phenomenon in discontinuous surfaces. However, such a phenomenon was possible to reduce by using the unique feature that digital holography have, this is the tomographic capability. Experimental results have proved reductions of these anomalies, 30%. Also, we have demonstrated a better tomographic capacity by using an ideal filter than Butterworth. Numerical simulation evidenced that the Talbot effect can also be present in VTF grating from 0 to 2 TPO. Also, we have shown that the size of the ideal low-pass filter in the holographic reconstruction process is dependent on focus zone. The results should be of interest to readers in the areas of optical metrology, grating diffraction, digital holography, and digital holographic microscopy.

5. Summary

DHM give us the possibility to scan biological samples, semitransparent materials and tissues in axial direction with nanometric resolution. This is possible because the technique have a unique characteristic of numerical refocusing or tomographic capacity. In this chapter, we have shown three application of this capacity. First, we extend the DOF of the MIO in order to

avoid topographical measurement error of a microlens of a 4.2 μm high. The compactness and easy-use of the MIO that we have presented not only DHMM as a new alternative to obtain digital holograms without spherical aberration and easy tilt correction in the phase image, but also that an easier, well-aligned, and insensitive to external vibrations setup is reached, in comparison with the typical setups. Second, we reduce the shot noise in phase and amplitude images coming from digital holograms. This reduction allows us to attain high topographic resolution comparable with an AFM results. Finally, we present a method to reduce noise in off-axis holograms when a Fourier filtering method is applied.

Acknowledgements

The support of FONDECYT (Preis 3140076, Preis 1140239 and Preis 1120764), FONDEF (Preis IT13I10034), CORFO (Preis 14BPC4-28651), USACH-DICYT ASOCIATIVO, SEP-PROMEP Preis 14146 F-38, and UTFSM-DGIP, CONICYT-PCHA/Doctorado Nacional 201363130065, is gratefully acknowledged. Some parts of the chapter are part of the previously published papers [18, 21, 22].

Author details

Miguel León-Rodríguez[1, 2]*, Juan A. Rayas-Alvarez[1], Amalia Martínez-García[3] and Raúl R. Cordero[1]

*Address all correspondence to: y_migue@hotmail.com

1 Universidad de Santiago de Chile, Santiago, Chile

2 Universidad Politécnica de Guanajuato, Cortazar, Guanajuato, Mexico

3 Centro de Investigaciones en Óptica, A.C. Loma del Bosque, León, Guanajuato, México

References

[1] Schnars U, Jüptner W. Direct recording of holograms by a CCD target and numerical reconstruction. Appl Opt. 1994;33(2):179–81.

[2] Baumbach T, Kolenovic E, Kebbel V, Jüptner W. Improvement of accuracy in digital holography by use of multiple holograms. Appl Opt. 2006;45(24):6077–85.

[3] Mann CJ, Yu L, Kim MK. Movies of cellular and sub-cellular motion by digital holographic microscopy. Biomed Eng Online. 2006;5:21.

[4] Charrière F, Kühn J, Colomb T, Montfort F, Cuche E, Emery Y, et al. Characterization of microlenses by digital holographic microscopy. Appl Opt. 2006;45(5):829–35.

[5] Kemper B, Stürwald S, Remmersmann C, Langehanenberg P, von Bally G. Characterisation of light emitting diodes (LEDs) for application in digital holographic microscopy for inspection of micro and nanostructured surfaces. Opt Lasers Eng. 2008;46(7):499–507.

[6] Ferraro P, Grilli S, Alfieri D, De Nicola S, Finizio A, Pierattini G, et al. Extended focused image in microscopy by digital Holography. Opt Express. 2005;13(18):6738–49.

[7] Colomb T, Pavillon N, Kühn J, Cuche E, Depeursinge C, Emery Y. Extended depth-of-focus by digital holographic microscopy. Opt Lett. 2010;35(11):1840–2.

[8] Kang X 康 新. An effective method for reducing speckle noise in digital holography. Chinese Opt Lett. 2008;6(2):100–3.

[9] Rong L戎路, Xiao W 肖文, Pan F 潘锋, Liu S 刘烁, Li R 李瑞. Speckle noise reduction in digital holography by use of multiple polarization holograms. Chinese Opt Lett. 2010;8(7):653–5.

[10] Charrière F, Rappaz B, Kühn J, Colomb T, Marquet P, Depeursinge C. Influence of shot noise on phase measurement accuracy in digital holographic microscopy. Opt Express. 2007;15(14):8818–31.

[11] Dubois F, Requena MN, Minetti C, Monnom O, Istasse E. Partial spatial coherence effects in digital holographic microscopy with a laser source. Appl Opt [Internet]. 2004;43(5): 1131–9. Available from: http://www.opticsinfobase.org/abstract.cfm?URI=ao-43-5-1131

[12] Kühn J, Charrière F, Colomb T, Cuche E, Montfort F, Emery Y, et al. Axial sub-nanometer accuracy in digital holographic microscopy. Meas Sci Technol. 2008;19(7):074007.

[13] Dubois F, Joannes L, Legros JC. Improved three-dimensional imaging with a digital holography microscope with a source of partial spatial coherence. Appl Opt. 1999;38(34):7085–94.

[14] Malacara D. Optical Shop Testing. Third. New Jersey: Wiley; 2007. pp. 696–731.

[15] Zhang T, Yamaguchi I. Three-dimensional microscopy with phase-shifting digital holography. Opt Lett. 1998;23(15):1221–3.

[16] J.W. G. Introduction to Fourier Optics. Second. New York: McGraw-Hill; 1996. 441 p.

[17] Ma S, Quan C, Zhu R, Tay CJ, Chen L, Gao Z. Application of least-square estimation in white-light scanning interferometry. Opt Lasers Eng. 2011;49(7):1012–8.

[18] León-Rodríguez M, Rodríguez-Vera R, Rayas JA, Calixto S. Digital holographic microscopy through a Mirau interferometric objective. Opt Lasers Eng. 2013;51(3):240–5.

[19] Colomb T, Kühn J, Charrière F, Depeursinge C, Marquet P, Aspert N. Total aberrations compensation in digital holographic microscopy with a reference conjugated hologram. Opt Express. 2006;14(10):4300–6.

[20] Goodman JW. Statistical Optics. New York: John Wiley & Sons; 1985.

[21] León-Rodríguez M, Rodríguez-Vera R, Rayas J a., Calixto S. High topographical accuracy by optical shot noise reduction in digital holographic microscopy. J Opt Soc Am A. 2012;29(4):498.

[22] León-rodríguez M, Rayas JA, Martínez-garcía A, Martínez-gonzalez A, Téllez-quiñones A, Flores-muñoz V. Reduction of the ringing effect in off-axis digital holography reconstruction from two reconstruction distances based on Talbot effect. Opt Eng. 2015;54(10):1041101–9.

[23] Cuche E, Marquet P, Depeursinge C. Simultaneous amplitude-contrast and quantitative phase-contrast microscopy by numerical reconstruction of Fresnel off-axis holograms. Appl Opt. 1999;38(34):6994–7001.

[24] Gonzalez RC, Woods RE, Eddins SL. Digital image processing using Matlab. Upper Saddle River, NJ: Woods, & Eddins; 2009.

[25] Ream N. Discrete-Time Signal Processing. Electronics and Power. Upper Saddle River, NJ: Prentice-Hall; 1999. 157 p.

[26] Creath K, Wyant J. Moiré and fringe projection techniques. Optical shop testing. Third. New Yersey: Elsevier Ltd; 1993. 653–685 p.

[27] Kim MS, Scharf T, Menzel C, Rockstuhl C, Herzig HP. Phase anomalies in Talbot light carpets of self-images. Opt Express [Internet]. 2013;21(1):1287–300. Available from: http://www.ncbi.nlm.nih.gov/pubmed/23389022

[28] El Mallahi A, Dubois F. Dependency and precision of the refocusing criterion based on amplitude analysis in digital holographic microscopy. Opt Express. 2011;19(7):6684–98.